

Absence of bulk charge density wave order in the normal state of UTe_2

C. S. Kengle^{1,2}, J. Vonka³, S. Francoual⁴, J. Chang⁵, P.
Abbamonte², M. Janoschek^{5,6}, P. F. S. Rosa¹, and W. Simeth^{1,5,6}

¹*Los Alamos National Laboratory, Los Alamos, NM 87545, USA*

²*Department of Physics, University of Illinois*

Urbana-Champaign, Urbana, Illinois, 61801, USA

³*Laboratory for X-ray Nanoscience and Technologies,*

Paul Scherrer Institute, Villigen PSI, Switzerland

⁴*Deutsches Elektronen-Synchrotron (DESY), D-22607 Hamburg, Germany*

⁵*Physik-Institut, Universität Zürich,*

Winterthurerstrasse 190, CH-8057 Zürich, Switzerland and

⁶*Laboratory for Neutron and Muon Instrumentation,*

Paul Scherrer Institute, Villigen PSI, Switzerland

A spatially modulated superconducting state at zero magnetic field, known as pair density wave (PDW), is a tantalizing state of matter with unique properties. PDWs have been observed in diverse spin-singlet superconductors ranging from high-temperature cuprate and Fe-based superconductors to kagome and two-dimensional chalcogenide compounds. Recent scanning tunneling microscopy (STM) studies reveal that spin-triplet superconductor UTe_2 hosts an unprecedented spin-triplet PDW whose wavevectors are indistinguishable from a preceding charge-density wave (CDW) order that survives to temperatures well above the superconducting critical temperature, T_c . Whether the PDW is the mother or a subordinate order remains unsettled. Here, based on a systematic search for bulk charge order above T_c using resonant elastic X-ray scattering (REXS), we show that the structure factor of charge order previously identified by STM is absent in the bulk within the sensitivity of REXS, which implies that the reported CDW order in the normal state of UTe_2 is a surface phenomenon. Our results invite two scenarios: either the density-wave orders condense simultaneously at T_c in the bulk, in which case PDW order is likely the mother phase, or these modulations are restricted to the surface.

I. INTRODUCTION

Unconventional superconductors not only provide a platform for the investigation of exotic pairing mechanisms beyond electron-phonon coupling, but already underpin existing technology such as powerful superconducting magnets or have potential for future applications such as topological quantum computing with fractionalized excitations. In particular, conventional s -wave superconductors are topologically trivial, whereas unconventional superconductors may be topological depending on the underlying SC order parameter. For any newly-discovered unconventional superconductor, the determination of its SC order parameter therefore becomes a central question. However, due to experimental discrepancies, disorder, and intertwined orders, such as charge-density waves (CDWs), magnetism, pair-density waves (PDWs), and nematicity, this is frequently challenging.

UTe_2 is a recent addition to the family of unconventional superconductors [1, 2], and its SC order parameter continues to defy consensus. Though there is strong evidence that

UTe₂ is a spin-triplet superconductor [3–6], reports of chiral, multicomponent, and topological superconductivity [7–10] have been challenged [11–15]. Recently, scanning tunneling microscopy (STM) measurements identified that the SC order parameter, $\Delta_q(\mathbf{k})$, is spatially modulated at three wave-vector components, \mathbf{q}_i ($i = 1, 2, 3$) which are around the Brillouin zone boundary [16]. This pair-density wave (PDW) is inherently linked to CDW order, ρ_q , which displays the same modulation components as Δ_q but shifted by a phase difference π [16–18].

Notably, CDW order survives to temperatures well above the superconducting critical temperature, $T_c \approx 1.6$ K. As discussed in Ref. [17], this intriguing result points to two possible scenarios of intertwined order: either the SC and PDW order parameters are dominant and generate subordinate charge modulations or the SC and CDW orders dominate and give rise to pair density modulations. In the first case, a superconducting gap energy of $250 \mu\text{eV}$ coupled to a $10 \mu\text{eV}$ PDW state must induce a CDW with a much larger energy scale of order 25 meV. In the second case, the normal-state CDW coexists with superconductivity below T_c to generate a $10 \mu\text{eV}$ PDW state at the same wavevectors. Gu *et al* argue that the second case is more plausible, whereas Aishwarya *et al* reason that a normal-state CDW is not inconsistent with a PDW mother phase because the PDW may melt into a CDW phase that survives to higher temperatures. Whether the PDW is the mother order or a subordinate order therefore remains unsettled.

Though STM is a powerful surface probe that provides both phase and domain sensitive information with high accuracy [19, 20], it is not inherently sensitive to ordered states in the bulk. As a result, STM alone is unable to make conclusive statements about correlation lengths of ordered states in the bulk of materials. In fact, signatures of CDWs observed in STM are equally likely to arise from bulk or surface states, and the two forms of order may coexist in a material [21]. Therefore, with all experimental evidence for either CDW or PDW modulations in UTe₂ being restricted to surface sensitive measurements, it remains unclear whether these modulations in the SC state extend into the bulk and, if so, whether the broadening of the momentum space CDW peaks above T_c is also a bulk phenomenon. Signatures of a phase transition when CDW order vanishes are absent in transport or thermodynamic measurements [22–24], therefore emphasizing the necessity to perform a systematic search for charge-density wave signatures using bulk-sensitive methods.

Here we provide the desired bulk measurements of the charge order in UTe₂ via resonant

elastic x-ray scattering (REXS) performed just above the superconducting transition ($T = 2.2$ K), which is about four times lower than the highest temperature the CDW in UTe_2 is reported to exist [18].

Because STM identified 5 nm-sized patches of charge order, we investigated a region in reciprocal space near two of the reported wave vectors with respect to broad signals of correlation lengths smaller than 5 nm using incident X-ray energies of 4.95 keV (Te L_1 edge) and 3.73 keV (U M_4 edge). Additionally, we investigated the vicinity of one of the ordering vectors on a tight grid sufficiently dense and large enough to identify resolution limited CDW-signals using incident X-ray energy of 3.73 keV. Our main result is that the structure factor of the putative CDW is absent from the bulk within our detection limits posed by state-of-the art X-ray diffraction.

II. RESULTS

A. Surface state observed in STM

We first revisit the nature of CDW order identified previously in STM studies. Sample volumes probed in STM are restricted to atomic length scales and extend, at best, over two atomic layers. STM is therefore not directly sensitive to modulation periods along the surface normal \mathbf{n} .

STM studies in Refs. [16–18] were performed on (011) surfaces. Here, the top layer consists of Te atoms forming a 2-D orthorhombic Bravais lattice with rectangular centered unit cell (cf. Supplementary Materials Text 1 and Figure S1). STM measurements below T_c identified superstructure-modulations, as inferred from Fourier transformed STM images, and concluded the presence of three ordering vectors (\mathbf{q}_1 , \mathbf{q}_2 , and \mathbf{q}_3) common to both CDW and PDW order. Fig. 1(a) shows these modulations schematically within the 2D Brillouin of the Te-lattice. Black circles correspond to the Fourier components of the lattice. Charge order peaks, shown in orange, form an isosceles triangle $\Delta_{\mathbf{q}_1\mathbf{q}_2\mathbf{q}_3}$ and are complemented to a mirror-symmetric pentagon $\mathbf{q}_1\mathbf{q}_2\mathbf{p}_1\mathbf{p}\mathbf{q}_3$ by the projections of \mathbf{q}_2 and \mathbf{q}_3 onto the x-axis (\mathbf{p} and \mathbf{p}_1).

Notably, the high symmetry points Y, Y_1 , L_2 , W, and L_1 at the boundary of the three-dimensional Brillouin zone of UTe_2 denoted by purple spheres form a pentagon of same

shape and of nearly equal size (cf. Fig. 1b). When projected onto the (011) plane, the images of W, L₁, and L₂ (represented by purple circles in Fig. 1a), almost coincide with the wave-vectors \mathbf{q}_1 , \mathbf{q}_2 , and \mathbf{q}_3 , suggesting therefore that the wave vectors of interest lie in the same plane at the Brillouin zone boundary.

Figure 1(b) shows an overview of the three-dimensional first Brillouin zone of UTe₂ wherein characteristic high-symmetry points are shown as spheres. The points W, L₁, and L₂, close to which the three wave-vectors were suspected, are colored purple. Here we use the labelling convention as in Ref. [16], describing the characteristic points, which in conventional orthorhombic coordinates are given by W($\frac{1}{2}, \frac{1}{2}, \frac{1}{2}$), L₁ (0.456, 0.596, 0), and L₂ (0.456, 0.404, 1). Charge order components are shown in terms of orange spheres and their location was inferred based on the assumption that they lie in the same reciprocal space layer as the points W, L₁, and L₂ at the Brillouin zone boundary.

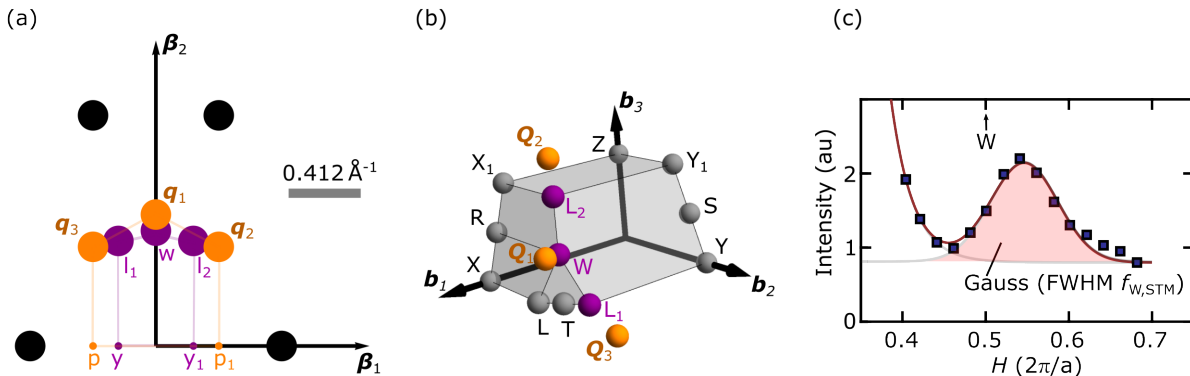


FIG. 1. **Multi-component surface-CDW identified by means of scanning tunneling microscopy.** (a) Schematic view of fast Fourier transformed STM images, as taken on (011) surfaces. The β_2 -axis is parallel to the crystallographic (100) axis of UTe₂ and β_1 is perpendicular to (100) and (011). Black circles indicate the Fourier components due to the lattice of Te-atoms. Large orange circles correspond to charge-ordered peaks, \mathbf{q}_1 , \mathbf{q}_2 , \mathbf{q}_3 . p and p₁ correspond to projections of \mathbf{q}_3 and \mathbf{q}_2 onto the x-axis. The purple spheres correspond to projections of high-symmetry points (denoted by the respective capital letters) within the three-dimensional Brillouin zone. (b) High-symmetry points in the first Brillouin zone of UTe₂, as represented by spheres. Ordering vectors were identified in the vicinity of W, L₁, and L₂ (purple spheres). The orange points correspond to the location of charge-ordered peaks within the (011) plane at the Brillouin zone boundary that have the projections that are shown in (a). (c) Exemplary cut along the line WS. Shown in terms of square symbols is intensity inferred from a fast Fourier transformation of STM picture taken at 4.9 K (cf. Fig. 2b of Ref. [18]). For the purposes in this study, we fitted the data by a superposition of exponentially decaying background and a Gaussian peak with FWHM $f_{\text{W,STM}}$ (brown lines). The Gaussian profile is shown in orange shading.

Above the superconducting transition temperature the charge order begins to melt. Charge order persists in the form of patches which shrink upon increasing temperature. For example, at 4.8 K the patches are of the order of 5 nm in size. Finally, the charge order in the superconducting state is field-dependent and vanishes at the same critical field, where superconductivity is suppressed, suggesting that SC and PDW order are coupled.

Fig. 1(c) shows a typical intensity *vs.* momentum curve obtained from a Fast Fourier Transformation (FFT) of STM images taken at 4.9 K along the line connecting the points W and S, *i.e.*, between $(\frac{1}{2}, \frac{1}{2}, \frac{1}{2})$ and $(\frac{1}{2}, \frac{1}{2}, 0)$ as specified in conventional orthorhombic coordinates. A pronounced peak near the W point arises from charge-density wave modulations and is characterized by a broad Gaussian profile centered at $h = 0.545$ r.l.u. The first wave-vector, $\mathbf{q}_1 = (0.545, 0.5, 0.5)$, is thus slightly off the W point and close to the ordering vector inferred from two dimensional Fourier transformations (See Supplementary Material Text 1 for more details). Similarly, ordering vectors close to L_1 and L_2 can be inferred from a detailed investigation of the STM pictures presented in Ref. [16]: $\mathbf{q}_2 = (0.430, 0.338, 1.339)$ and $\mathbf{q}_3 = (0.430, 0.662, -0.339)$, which do not match any obvious commensurate value.

Finally, we use the STM data to infer a conservative estimation of the expected full width at half maximum (FWHM) of bulk CDW order. Consider that the peak FWHM seen in STM represents a convolution of intrinsic peak shape ($f_0 = 2/\kappa_0$), associated with the correlation length κ_0 of CDW order, and the experimental resolution of the STM instrument, (f_{STM}). Assuming that both f_0 and f_{STM} describe the widths of Gaussian profiles, we find that the profile in Fig. 1(b) has a FWHM $f_{\text{W,STM}} = \sqrt{f_0^2 + f_{\text{STM}}^2}$. The experimental profile therefore serves as an upper bound for the internal width of charge-order, yielding $f_{\text{max}} := f_{\text{W,STM}} = 0.1439 \text{ \AA}^{-1} > f_0$. A lower bound may be obtained considering that coherent CDW correlations were observed in terms of patches of less than $\kappa_1 = 5$ nm diameter, implying a lower bound for the intrinsic peak width of $f_{\text{min}} := 2/\kappa_1 < f_0$, cf. Ref. [25]. Combined, these limits on the FWHM can be written $f_{\text{min}} = 0.04 \text{ \AA}^{-1} < f_0 < 0.1439 \text{ \AA}^{-1} = f_{\text{W,STM}}$.

B. Resonant X-ray scattering

To study bulk microscopic properties of charge modulations in UTe_2 , we utilized resonant elastic scattering of hard X-rays and searched for signatures of a multi-component CDW, as reported previously to exist at the Brillouin zone boundary. With penetration depths in

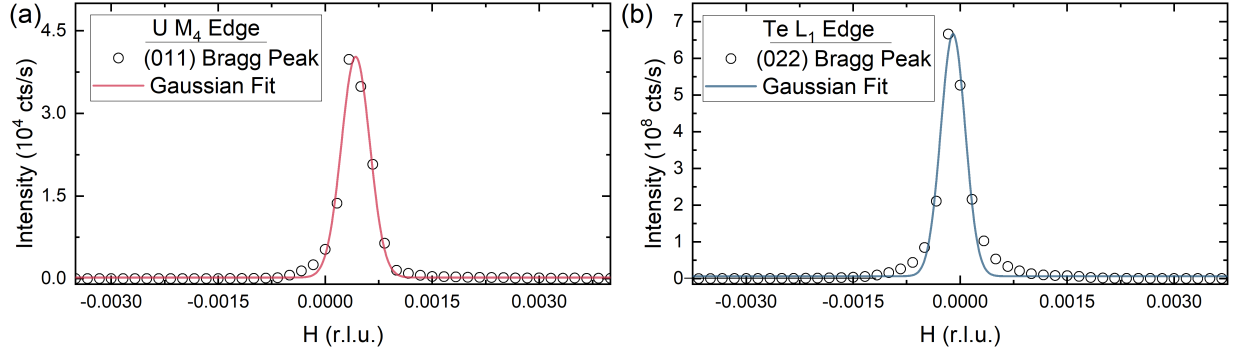


FIG. 2. Resolution-limited structural Bragg peaks. (a) At incident energy of 3.73 keV, the FWHM is 4.6985×10^{-4} r.l.u. = $6.85 \times 10^{-4} \text{ \AA}^{-1}$ (b) At incident energy of 4.95 keV, the FWHM is 3.07×10^{-4} r.l.u. = $4.68 \times 10^{-4} \text{ \AA}^{-1}$.

UTe₂ exceeding 200 nm, these experiments are sensitive to the structure factor of long-range correlations across several hundred crystallographic unit cells. Bragg scattering at charge-order peaks is typically studied with non-resonant scattering and characteristically leaves incident polarization invariant. The beam can be linearly polarized perpendicular to the scattering plane, σ , or perpendicular to the scattering plane, π .

For the putative resonant enhancement of charge-density wave order, the structure factor is unknown, but may have finite contributions in any polarization channel. Therefore, the chance to observe charged-ordered Bragg peaks may be maximized when polarization is maintained parallel to the scattering plane, i.e., using the $\sigma\sigma'$ -channel. In our experiments, structural Bragg peaks measured on UTe₂ were limited by experimental resolution represented by Gaussian profiles, indicating ideal crystalline quality. Figure 2 shows representative scans through (a) the (011) Bragg peak using an incident energy of 3.73 keV and (b) the (022) Bragg peak using an incident energy of 4.95 keV. See Supplementary Information for more details on the setup of our diffraction experiments.

C. Survey for putative CDW order in bulk

To search for the CDW in the bulk, we will consider two limits. First, that the CDW peaks are resolution limited (having the same resolution as the structural Bragg peaks). Next, that the CDW has correlation lengths of order 5 nm, inspired by previous STM measurements [18].

We start with the search for resolution-limited charge-order peaks. We surveyed reciprocal

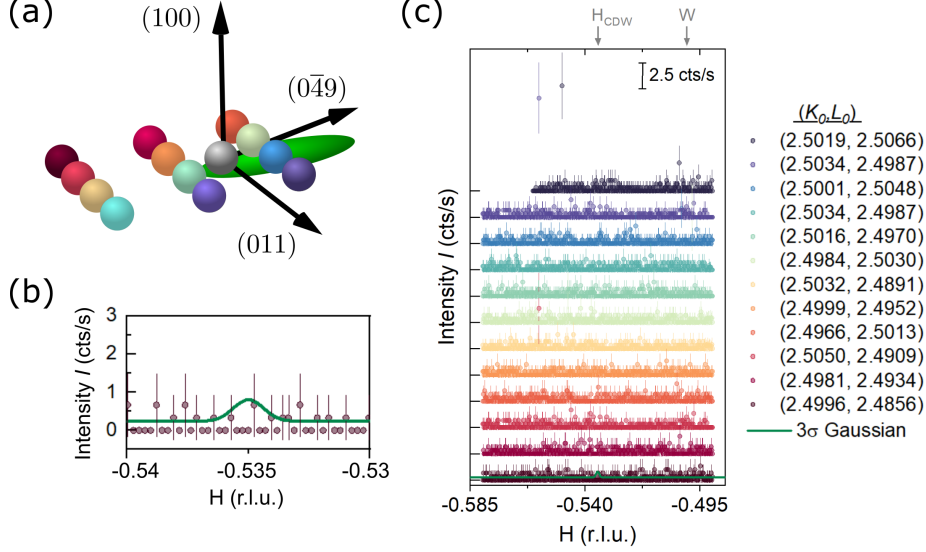


FIG. 3. **Absence of resolution-limited CDW Bragg peaks near \mathbf{q}_1 .** (a) Reciprocal space region that was investigated by means of H -scans. K_0 and L_0 coordinates were held constant during each scan and are illustrated in terms of colored spheres. The grey sphere denotes the W-point, the projection where the CDW-peak is expected according to STM. The green ellipsoid illustrates the resolution of the diffractometer. (b) H scan at $(K, L) = (2.4996, 2.4856)$, zoomed in to emphasize the shape of a resolution-limited Gaussian of height 3σ . (c) REXS intensity of all H -scans. Colors denote the K_0, L_0 -coordinates in (a). Plots are offset for clarity, and each horizontal line indicates zero for the corresponding plot. The intensity scale of 2.5 cts/s is indicated by the black scale bar.

space in search of signal at $\mathbf{Q}_{1,a}^{\text{CDW}} = (-0.54, 2.5, 2.5)$, corresponding to CDW wave-vector of type \mathbf{q}_1 in STM, shown by the grey sphere in Fig. 3(a). The letter a denotes the specific momentum transfer, where the CDW peak was studied in our experiments. Such charge order would be detected when correlation lengths are larger than $2/f_{\text{res}}$, where f_{res} denotes the width in momentum space of resolution-limited structural Bragg peaks. We therefore chose an incident energy of 3.37 keV, where resolution volumes are maximal.

To account for possible uncertainty in the CDW position, we perform a 3-dimensional grid search at positions near \mathbf{q}_1 . The mesh grid coordinates (colored spheres in Fig. 3(a)) are spaced 0.0018 r.l.u apart in k and l , which is smaller than the instrument resolution (green ellipsoid in Fig. 3(a)) to maximize the chance of detecting a resolution-limited CDW peak. The mesh consists of H -scans at given K_0, L_0 -coordinates indicated in Fig. 3. The step width, $\Delta H = 3.6 \cdot 10^{-4} \text{ \AA}^{-1}$, is smaller by a factor of two than the experimental resolution determined for a nearby specular Bragg peak (c.f. Supplementary Material Text 3).

Figure 3(c) shows the resulting scans, where the color of the plot corresponds to the

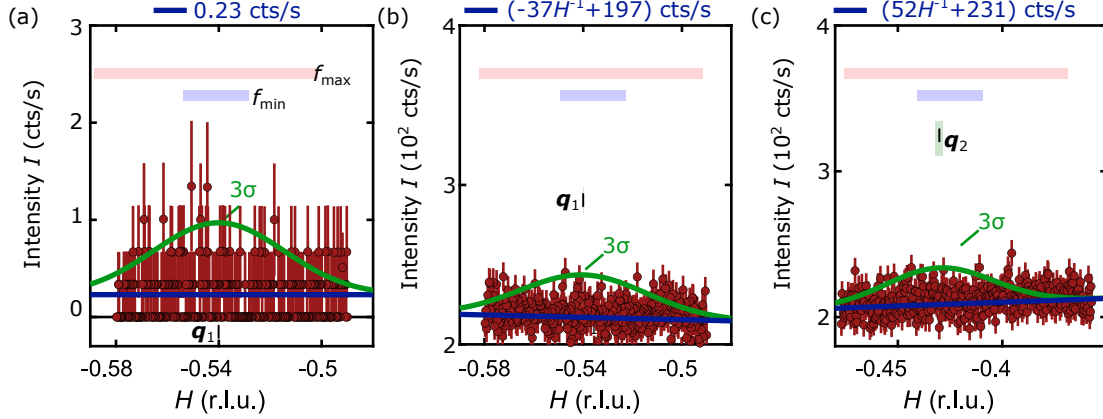


FIG. 4. **Absence of diffuse charge-scattering peaks in resonant X-ray diffraction data.** The three panels show momentum-space cuts through positions, where according to STM reports diffuse charge scattering peaks of a multi-component CDW above the superconducting transition were reported. Shown in (a) is an H scan through \mathbf{q}_1 ($H, 2.5, 2.5$) using 3.73 keV incident energy, in (b) through \mathbf{q}_1 ($H, 3.5, 3.5$) using 4.95 keV incident energy, and in (c) through \mathbf{q}_2 ($H, 2.338, 2.661$) using incident energy 4.95 keV. As explained in the text and derived from STM, a diffuse CDW signal may be expected to have full width have maximums in the interval $f_{\min} = 0.04 \text{ \AA}^{-1} < f_0 < 0.1439 \text{ \AA}^{-1} = f_{\max}$. The red circles present X-ray counts, where the error bars correspond to uncertainties arising from Poisson counting statistics. Points at zero intensity are here shown with vanishing error bars. The background was fitted by linear functions (blue thick line). The green line corresponds to a Gaussian peak with an amplitude of 3σ above the background, where σ denotes the mean error bar of the X-ray counts.

K_0, L_0 -coordinates in (b). The scans can be modeled by only a constant background of 0.23(1) cts/s with averaged standard error from Poisson counting statistics of $\sigma = 0.19$ cts/s. As a conservative upper limit of the maximum intensity due to charge modulations, we assume that one would be able to detect signatures that are three error bars above the background (in the following denoted “ 3σ ”).

As such a signal was not observed (green curve), we conclude that the maximum CDW amplitude at 3.73 keV incident energy is below our 3σ limit: $A(\mathbf{Q}_{1,a}^{\text{CDW}}) \leq 0.61$ cts/s. Comparing to the peak height of a nearby Bragg peak, (0,1,1), we find that the its CDW peak amplitude is at least five orders of magnitude lower $A_{\text{CDW}} \leq 1.5 \cdot 10^{-5} \cdot A_{(0,1,1)}$.

Turning now to the second scenario, where CDW peaks have \sim nm-sized short correlation lengths, we expand our search to look for signal at the corresponding bulk positions of \mathbf{q}_1 and \mathbf{q}_2 . For wavevector \mathbf{q}_1 , data was collected in two Brillouin zones using two incident energies: $\mathbf{Q}_{1,a}^{\text{CDW}} = (-0.54, 2.5, 2.5)$ at 3.73 keV and $\mathbf{Q}_{1,b}^{\text{CDW}} = (-0.54, 3.5, 3.5)$ at 4.95 keV. Here b labels another momentum-transfer, where we studied the respective wave-vector. For

wavevector \mathbf{q}_2 , scans were taken in one Brillouin zone at $\mathbf{Q}_{2,b}^{\text{CDW}} = (-0.430, 2.338, 2.661)$ with incident energy of 4.95 keV.

Our scan results at both incident energies and wavevectors are presented in Fig. 4. Panels (a) and (b) show scans at \mathbf{q}_1 at 3.73 keV and 4.95 keV, respectively, and panel (c) shows scans at \mathbf{q}_2 at 4.95 keV.

The background intensities were each fitted using a line with a constant slope and offset, shown in blue. The fit results are displayed above each panel. Mean error bars, σ , as obtained from Poisson counting statistics are given by (a) 0.17 cts/s, (b) 8.9 cts/s, and (c) 8.38 cts/s.

A charge ordered peak having a FWHM of $(f_{\min} + f_{\max})/2$ and amplitude $\geq 3\sigma$ would be detectable above the background, as indicated by the green Gaussian curves in Fig. 4. We conclude that such Gaussian profiles are absent within our detection limit in all three cases.

Comparison of intensities lets us conclude that the maximum intensities of CDW peaks having short correlation lengths in bulk are at least eight orders of magnitude smaller than for the structural Bragg peaks.

D. Upper boundary on atomic displacements

Charge modulations probed by Thomson scattering of X-rays can arise either from spatial modulation of valence electrons or from periodic atomic displacements [26]. These two effects typically appear together. With periodic lattice displacements leading to a much stronger response in X-ray scattering, we consider them as indirect evidence of valence modulations [27]. Here, we will calculate the limits of atomic displacements in UTe_2 based on the scattering intensities reported above.

Using standard expressions, displacements of atoms along a direction \mathbf{d} away from the equilibrium position \mathbf{r}_i may be written as $\mathbf{r}'_i = \mathbf{r}_i + u\hat{\mathbf{d}} \cdot \sin(\mathbf{q}_0 \cdot \mathbf{r}_i)$. In diffraction, this leads to charge-order Bragg peaks around structural Bragg peaks \mathbf{q} , appearing in leading order at $\mathbf{G} \pm \mathbf{q}_0$.

The structure factor of the modulated crystal can accordingly be written as

$$S(\mathbf{Q}) = \sum_{\mathbf{G}} \delta(\mathbf{Q} - \mathbf{G}) + i \left(\frac{\mathbf{Q} \cdot \mathbf{u}}{2} \right) \sum_{\mathbf{G}} \left[\delta(\mathbf{q} + \mathbf{q}_0 - \mathbf{G}) + \delta(\mathbf{q} - \mathbf{q}_0 - \mathbf{G}) \right] \quad (1)$$

and is related to the measured quantities given that the structure factor is proportional to the integrated intensities of Bragg peaks, i.e., $I(\mathbf{Q}) \propto |S(\mathbf{Q})|^2$. The ratio of intensities of a structural Bragg peak to a charge order Bragg peak yields

$$\frac{I(\mathbf{q}_0 + \mathbf{G})}{I(\mathbf{G})} = \left(\frac{\mathbf{u} \cdot (\mathbf{q}_0 + \mathbf{G})}{2} \right)^2 \quad (2)$$

The intensity at CDW position in momentum space may arise from a combination of two domains. For example, at momentum $\mathbf{Q}_{1,a}^{\text{CDW}} = (-0.545, 2.5, 2.5)$, the intensity arises from CDW modulations with wave-vector component $(-0.545, 0.5, 0.5)$ of the $\mathbf{G}_1 = (0, 2, 2)$ zone and with $(-0.545, -0.5, -0.5)$ of the $\mathbf{G}_2 = (0, 3, 3)$ zone, two different representatives of the \mathbf{q}_1 -modulation. Calculation of the crystal structure factor of UTe_2 permits comparison with the intensity of the structural Bragg peak at $\mathbf{G}_0 = (0, 1, 1)$ and yields

$$\left(\frac{\mathbf{u} \cdot \mathbf{Q}_0^{\text{CDW}}}{2} \right)^2 = \frac{A(\mathbf{Q}_{1,a}^{\text{CDW}}) \cdot V(\mathbf{Q}_{1,a}^{\text{CDW}})}{A(\mathbf{G}_0) \cdot V(\mathbf{G}_0)} \cdot \frac{S(\mathbf{G}_0)}{S(\mathbf{G}_1) + S(\mathbf{G}_2)}. \quad (3)$$

We first look at the measurements taken at 3.37 keV shown in Sec. II C. For resolution-limited CDW peaks the maximum atomic displacements can be estimated using the above equation. Along the (100) direction we determine $u_{\parallel(100)} \leq 4.7 \cdot 10^{-3} \text{ \AA}$ and along the (110) direction $u_{\parallel(011)} \leq 1.2 \cdot 10^{-3} \text{ \AA}$. In comparison, the atomic displacements in the CDW in $\text{YBa}_2\text{Cu}_3\text{O}_{6.67}$ is of order $u \approx 3 \cdot 10^{-3} \text{ \AA}$ [27], or similarly $u \approx 10^{-3} \text{ \AA}$ in related compounds [28].

Now we turn to the data shown in Fig. 4, where we have assumed short correlation lengths for the CDW. Again using Eq. 3 with consideration of multiple domains, we can find upper bounds for displacement amplitudes of CDWs having widths $f_{\text{CDW}} = (f_{\text{min}} + f_{\text{max}})/2 = 0.09 \text{ \AA}^{-1}$. Since the CDW peak width is much larger than the REXS momentum resolution, the integration volume is essentially resolution independent: $V(\mathbf{Q}_{\text{CDW}}) = (f_{\text{CDW}}^2 + f_{\text{res}}^2)^{3/2} \approx f_{\text{CDW}}^3$.

Considering Fig. 4(b), we find that atomic displacements at 4.95 keV incident energy are limited by $u \leq 0.22 \text{ \AA}$ along the (100) direction and $u \leq 0.06 \text{ \AA}$ along the (011) direction. Considering instead Fig. 4(a), we find that for \mathbf{q}_1 at incident energy of 3.73 keV, the atomic displacements are limited by $u < 0.33 \text{ \AA}$ along (011) and $u \leq 1.2 \text{ \AA}$ along the (100) direction,

therefore providing a weaker bound. While these numbers are larger than seen in the cuprates, the order in UTe_2 for this case is localized and would represent inhomogeneity in the CDW state throughout the sample.

III. DISCUSSION

Our measurements using resonant X-rays show that the charge modulations earlier observed in STM above the superconducting transition at the surface of UTe_2 are absent from the bulk within our detection limits posed by state-of-the art X-ray diffraction. Our measurements were performed at $T = 2.2$ K, about four times lower than the highest temperature the CDW in UTe_2 is reported to exist [18]. Our results did not reveal diffraction intensity in the vicinity of the CDW wave vectors at either the U M_4 or Te L_1 absorption edges that is noticeable above the background level.

The coverage of our fine mesh-grid search near the \mathbf{q}_1 CDW wave vector rules out the possibility that the CDW peak is too sharp to be observed in bulk X-ray measurements. Notably, the maximum diffraction intensity of long-ranged CDW is at least five orders of magnitude smaller relative to the intensity of the strongest Bragg peaks observed. Atomic displacements of long-range modulations with resolution limited Bragg signatures are four orders of magnitude smaller than the respective atomic units along (100) and (011).

We investigated regions in reciprocal space large enough using step-widths fine enough in order to rule out the presence of CDW peaks with short correlation lengths in the bulk. Comparing REXS intensities, we find that integrated intensities of putative bulk CDW peaks are at least eight orders of magnitude weaker than nearby structural Bragg peaks. We conclude that in the case of putative broad CDW peaks, maximum atomic displacements are two orders of magnitude smaller than the respective crystallographic unit for both (100) and (011) reciprocal directions.

We highlight that neither thermodynamic measurements [22–24] nor inelastic neutron scattering identified any signatures suggestive of bulk charge order above the superconducting transition [29–32]. In combination with our results, the emergence of a surface charge-density wave in the normal state provides the most consistent picture. As for the superconducting state, our results point to two possible conclusions: either the density-wave orders condense simultaneously at T_c in the bulk, in which case PDW order is likely the

mother phase, or these modulations are restricted to the surface. Bulk scattering measurements in the superconducting state are required to address this outstanding question.

IV. MATERIALS AND METHODS

Sample Preparation For our experiments, a single crystal of UTe_2 with a superconducting transition at $T_C = 1.8 \text{ K}$ (cf. Ref. [24]), was used. The sample was oriented with the (100) axis horizontal within 2° using Laue backscattering. See Supplemental Material Figure S. 2. The sample surface was the (011) plane, with a surface normal 24° away from the (001) direction and 66 deg away from the (010) direction. The sample was mounted to a copper holder using room-temperature cure silver epoxy and allowed to cure for > 3 days in an Ar environment. Aluminum cleave pins were glued to the tops of the samples with TorrSeal and allowed to cure for 1 day in an a Ar environment. Prior to measurement the samples were cleaved, then immediately transferred to vacuum to avoid surface contamination and degradation.

Resonant Elastic X-ray Scattering Experiments were carried out in the second experimental hutch EH2 of beamline P09 at the synchrotron source PETRA III [33]. The X-ray diffraction was carried out in a horizontal scattering geometry. The UTe_2 sample was cooled using a variable temperature insert in a cryomagnet able to provide magnetic fields up to 14 T. X-rays with incident linear polarization were chosen using phase plates [34].

Structural Bragg peaks measured on UTe_2 essentially featured Gaussian profiles. Their intensity may be modelled by:

$$G(\mathbf{Q}) := A \cdot E(\mathbf{Q}) \tag{4}$$

where A denotes the amplitude (or the maximum) and E is a Gaussian profile with full width at half maxima f_{d_1} , f_{d_2} , and f_{d_3} along the three directions $\mathbf{d}_1 = (1, 0, 0)$, $\mathbf{d}_2 = (0, 1, 1)$, and $\mathbf{d}_3 = (0, 0, 0)$, respectively. Integrated intensity of a Bragg peak is therefore given by $I = \frac{1}{8} \sqrt{\frac{\pi}{\ln(2)}}^3 \cdot A f_{d_1} f_{d_2} f_{d_3}$. The profile of structural Bragg peaks is essentially restricted by resolution. We therefore define $f_{d_1} f_{d_2} f_{d_3}$ as the experimental resolution volume in momentum space.

Data Availability The datasets generated during and/or analysed during the current

study are available from the corresponding author on request.

Acknowledgments

WS acknowledges fruitful discussions with Aline Ramirez. WS was supported through funding from the European Union's Horizon 2020 research and innovation programme under the Marie Skłodowska-Curie grant agreement No 884104 (PSI-FELLOW-III-3i). Work at Los Alamos National Laboratory was performed under the auspices of the U.S. Department of Energy, Office of Basic Energy Sciences, Division of Materials Science and Engineering. C.S.K. acknowledges support from the Laboratory Directed Research and Development program. P.A. acknowledges support from the Gordon and Betty Moore Foundation, EPiQS grant GBMF9452. J. C. acknowledges support from Swiss National Science foundation under grant 200021-188564. MJ acknowledges funding by the Swiss National Science Foundation through the project "Berry-Phase Tuning in Heavy f-Electron Metals" (200650). We acknowledge DESY (Hamburg, Germany), a member of the Helmholtz Association HGF, for the provision of experimental facilities. Parts of this research were carried out at PETRA III at DESY. Beamtime was allocated for proposal I-20221340 EC.

Author information

The authors declare no competing financial interests. Correspondence and requests for materials should be addressed to ckengle@lanl.gov and wsimeth@lanl.gov.

-
- [1] Ran, S. et al. Nearly ferromagnetic spin-triplet superconductivity. Science **365**, 684–687 (2019).
- [2] Aoki, D. et al. Unconventional superconductivity in heavy fermion UTe_2 . Journal of the Physical Society of Japan **88**, 1–5 (2019).
- [3] Matsumura, H. et al. Large Reduction in the a-axis Knight Shift on UTe_2 with $T_c = 2.1$ K. Journal of the Physical Society of Japan **92**, 063701 (2023).
- [4] Nakamine, G. et al. Superconducting properties of heavy fermion UTe_2 revealed by ^{125}Te -nuclear magnetic resonance. Journal of the Physical Society of Japan **88**, 113703 (2019).
- [5] Ran, S. et al. Extreme magnetic field-boosted superconductivity. Nature Physics **15**, 1250–1254 (2019).
- [6] Knebel, G. et al. Field-reentrant superconductivity close to a metamagnetic transition in the heavy-fermion superconductor UTe_2 . Journal of the Physical Society of Japan **88**, 063707 (2019).
- [7] Jiao, L. et al. Chiral superconductivity in heavy-fermion metal UTe_2 . Nature **579**, 523–527 (2020).
- [8] Hayes, I. et al. Multicomponent superconducting order parameter in UTe_2 . Science **373**, 797–801 (2021).
- [9] Wei, D. S. et al. Interplay between magnetism and superconductivity in UTe_2 . Phys. Rev. B **105**, 024521 (2022).
- [10] Ishihara, K. et al. Chiral superconductivity in UTe_2 probed by anisotropic low-energy excitations. Nature Communications **14**, 2966 (2023).
- [11] Thomas, S. M. et al. Spatially inhomogeneous superconductivity in UTe_2 . Phys. Rev. B **104**, 224501 (2021).
- [12] Theuss, F. et al. Single-Component Superconductivity in UTe_2 at Ambient Pressure (2023). 2307.10938.
- [13] Li, Z. et al. Observation of odd-parity superconductivity in UTe_2 (2023). 2309.08668.
- [14] Ajeesh, M. O. et al. Fate of time-reversal symmetry breaking in ute_2 . Phys. Rev. X **13**, 041019 (2023).
- [15] Iguchi, Y. et al. Microscopic Imaging Homogeneous and Single Phase Superfluid Density in

- UTe₂. Phys. Rev. Lett. **130**, 196003 (2023).
- [16] Aishwarya, A. et al. Magnetic-field-sensitive charge density waves in the superconductor UTe₂. Nature **618**, 928 (2023).
- [17] Gu, Q. et al. Detection of a pair density wave state in UTe₂. Nature **618**, 921 (2023).
- [18] LaFleur, A. et al. Inhomogeneous high temperature melting and decoupling of charge density waves in spin-triplet superconductor UTe₂ (2023). 2308.03721.
- [19] Carpinelli, J. M., Weitering, H. H., Plummer, E. W. & Stumpf, R. Direct observation of a surface charge density wave. Nature **381**, 398–400 (1996).
- [20] Thomson, R. E., Burk, B., Zettl, A. & Clarke, J. Scanning tunneling microscopy of the charge-density-wave structure in 1T-TaS₂. Phys. Rev. B **49**, 16899–16916 (1994).
- [21] Li, H. et al. Discovery of conjoined charge density waves in the kagome superconductor CsV₃Sb₅. Nat Commun **13**, 6348 (2022).
- [22] Metz, T. et al. Point-node gap structure of the spin-triplet superconductor UTe₂. Phys. Rev. B **100**, 220504 (2019).
- [23] Sakai, H. et al. Single crystal growth of superconducting UTe₂ by molten salt flux method. Phys. Rev. Mater. **6**, 073401 (2022).
- [24] Rosa, P. F. et al. Single thermodynamic transition at 2 K in superconducting UTe₂ single crystals. Nature Communications Materials **3**, 33 (2022).
- [25] Kindervater, J. et al. Weak Crystallization of Fluctuating Skyrmion Textures in MnSi. Phys. Rev. X **9**, 041059 (2019).
- [26] Abbamonte, P. Charge modulations versus strain waves in resonant x-ray scattering. Physical Review B **74**, 195113 (2006). URL <https://link.aps.org/doi/10.1103/PhysRevB.74.195113>. Publisher: American Physical Society.
- [27] Chang, J. et al. Direct observation of competition between superconductivity and charge density wave order in YBa₂Cu₃O_{6.67}. Nature Physics **8**, 871–876 (2012). URL <https://www.nature.com/articles/nphys2456>. Number: 12 Publisher: Nature Publishing Group.
- [28] Forgan, E. M. et al. The microscopic structure of charge density waves in underdoped YBa₂Cu₃O_{6.54} revealed by X-ray diffraction. Nat Commun **6**, 10064 (2015).
- [29] Duan, C. et al. Incommensurate Spin Fluctuations in the Spin-Triplet Superconductor Candidate UTe₂. Phys. Rev. Lett. **125**, 237003 (2020).

- [30] Duan, C. *et al.* Resonance from antiferromagnetic spin fluctuations for superconductivity in UTe_2 . Nature **600**, 636–640 (2021).
- [31] Butch, N. P. *et al.* Symmetry of magnetic correlations in spin-triplet superconductor UTe_2 . npj Quantum Materials **7**, 39 (2022).
- [32] Knafo, W. *et al.* Low-dimensional antiferromagnetic fluctuations in the heavy-fermion paramagnetic ladder compound UTe_2 . Phys. Rev. B **104**, L100409 (2021).
- [33] Stempfer, J. *et al.* Resonant scattering and diffraction beamline P09 at PETRA III. J Synchrotron Rad **20**, 541 (2013).
- [34] Francoual, S., Stempfer, J., Reuther, D., Shukla, D. K. & Skaugen, A. Double phase-retarder set-up at beamline P09 at PETRA III. J. Phys.: Conf. Ser. **425**, 132010 (2013).